Thermal effect on drainage flow of a viscous gas from a semisealed narrow channel

Wei Huang and Kang Ping Chen*
School for Engineering of Matter, Transport and Energy, Arizona State University, Tempe, Arizona 85287-6106, USA

(Received 15 April 2019; published 12 August 2019)

Drainage flow of a viscous compressible gas from a semisealed narrow conduit is a pore-scale model for studying the fundamental flow physics of fluid recovery from a porous reservoir without fluid injection. The drainage flow is driven by the volumetric expansion of the gas and its mass flow rate has been found previously to be sliplike and proportional to the kinematic viscosity of the gas. Thermal effect on such a drainage flow is studied here by simultaneously solving the linearized continuity, momentum, and energy equations for a semisealed narrow channel with adiabatic walls. It is shown that even in the absence of an imposed temperature drop, gas expansion induces a transient temperature decrease inside the channel, which slows down the drainage process compared to the isothermal model and Lighthill's model. For a given density drop, gas drains out faster as the initial-to-final temperature ratio increases; the transient density can undershoot the final equilibrium value. It is concluded that thermal effect should be carefully considered in order to accurately predict the drainage rate.

DOI: 10.1103/PhysRevFluids.4.084202

I. INTRODUCTION

During the early stage of fluid recovery from a petroleum reservoir, volumetric expansion of the sedimentary rock is negligible due to its large bulk modulus and a small drawdown in the pressure of the *in situ* fluid. If no fresh fluid is injected into the reservoir to displace the *in situ* fluid, fluid recovery then relies entirely on the volumetric expansion of the *in situ* fluid and this so-called primary recovery period can last up to several years [1,2]. A fundamental pore-scale prototype problem for such a recovery process is the drainage flow of a viscous compressible gas from a long and narrow semisealed capillary or channel: the capillary or channel is initially filled with a gas of high density ρ_i and the unsealed end is opened at $t = 0$ with a prescribed lower density ρ_e at the exit (Fig. 1). As demonstrated by Chen and Shen [3–5], the solution to this volumetric-expansion-driven pore-scale drainage flow provides intriguing insights into the physics of the drainage process. Chen and Shen [3–5] solved the linearized compressible Navier-Stokes equations subject to the no-slip condition. Their results show that at large times relative to the period of acoustic oscillation, the mass production rate from a very narrow conduit is proportional to the kinematic viscosity of the gas. The mass production rate of this no-slip flow is also sliplike, as it is proportional to the square of the capillary radius (or linearly proportional to the channel gap). These pore-scale results differ fundamentally from those for the familiar Poiseuille type of flow, which produces a mass flow rate *inversely* proportional to the fluid's kinematic viscosity but proportional to the quartic of the pore radius (or the cubic of the channel gap). The Poiseuille flow mechanism of pushing a fluid through a conduit (displacement type) is completely absent in a semisealed conduit. The reason that

*k.p.chen@asu.edu

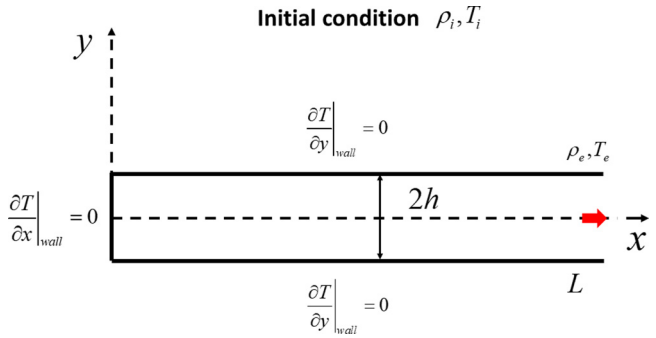

FIG. 1. Schematic for drainage flow from a semisealed microchannel with adiabatic walls. The end at $x = L$ is opened at $t = 0$ with the exit maintained at a density lower than the initial density.

the mass flow rate is proportional to the kinematic viscosity is that in the limit of a very narrow tube (channel), the flow is dominated by the self-diffusion effect of the viscous compressible gas and the self-diffusion coefficient is proportional to the kinematic viscosity [3,5–7]. Thermal effect, however, has been completely neglected in these studies despite the fact that the flow is solely driven by the density change of the gas. For a compressible gas, a temperature change always accompanies a density change; these changes can be of the same order of magnitude. Therefore, the thermal effect should be expected to have a significant influence on the drainage rate. Furthermore, in shale formations, as much as 75% of the total gas in place is adsorbed gas on the surface of organic pores [8]. Since the gas desorption rate is sensitive to temperature change, harvesting this large amount of adsorbed gas from shale requires a good understanding of the temperature change at the pore scale during the drainage process.

It is noted that there are many recent studies on microscale gas flows such as [9–11], some of which have included the thermal effect. These works as well as many others (the list is too long to be referenced here), however, deal with the displacement type of flow, which differs fundamentally from the volumetric-expansion-driven drainage flow as discussed above. The objective of the current work is to study the thermal effect on the volumetric-expansion-driven pore-scale drainage flow of a viscous compressible gas from a semisealed narrow channel by simultaneously solving the continuity, momentum, and energy equations. For small perturbations of an equilibrium state, we linearize the governing equations and utilize the Helmholtz decomposition theorem to split the perturbations to the longitudinal, thermal, and transverse modes. Since drainage flow from a semisealed channel is driven by the volumetric expansion of the gas, the longitudinal and thermal modes control the drainage process, while the role of the solenoidal transverse mode is to ensure that the overall velocity satisfies the no-slip condition on the channel walls [3–5]. In theory, a variety of thermal conditions on the conduit wall can be considered. In the present study, however, we only focus on the adiabatic wall condition for the following reason: Density change in the semisealed channel completely determines the drainage rate at the exit. In the studies neglecting the thermal effect [3–5], the solution for the density is a plane wave (independent of the transverse coordinate); thus, an initial assessment on the thermal effect would be to consider also a plane-wave solution that includes the thermal effect. Such a plane-wave solution in the presence of the thermal effect is only possible when the walls are adiabatic. Thus, due to the complexity of the thermal coupling, as a first step, we only study the nontrivial features brought out by the thermal effect for this particular class of solution and defer consideration of other thermal boundary conditions to a follow-up study. For adiabatic walls, an analytical solution for the nonisothermal drainage flow is obtained for the longitudinal and thermal modes, while the transverse mode is obtained numerically. It will be shown that, even when there is no imposed temperature drop, the transient temperature inside the channel falls below the equilibrium temperature due to gas expansion during the drainage process. On

the other hand, for any imposed temperature drop, the transient temperature inside the channel stays above the final equilibrium temperature, but the transient density can undershoot the final equilibrium value when the initial-to-final temperature ratio is large. The results for the excess mass inside the channel indicate that the isothermal model and the phenomenological model of Lighthill [9] are likely to provide inaccurate predictions of the mass flow rate for this class of nonisothermal drainage flow.

II. GOVERNINING EQUATIONS FOR THE NONISOTHERMAL DRAINAGE FLOWS OF AN IDEAL GAS

The continuity, momentum, and energy equations for a viscous compressible Newtonian fluid obeying Fourier's law of heat conduction are [12]

$$\frac{\partial \rho}{\partial t} + \nabla \cdot (\rho \mathbf{v}) = 0, \tag{2.1}$$

$$\rho \frac{D\mathbf{v}}{Dt} = -\nabla p + (\mu_b + \mu/3)\nabla(\nabla \cdot \mathbf{v}) + \mu \nabla^2 \mathbf{v}, \tag{2.2}$$

$$\rho c_p \frac{DT}{Dt} = \nabla \cdot (\kappa \nabla T) + \beta T \frac{Dp}{Dt} + \Phi_d, \tag{2.3}$$

where D/Dt is the material derivative; $\mathbf{v}$, p, ρ are the velocity, pressure, and density; μ, μ_b, c_p, κ are the shear viscosity, bulk viscosity, constant-pressure specific heat, and thermal conductivity of the fluid, respectively; all of these fluid properties are assumed to be constants. β is the thermal expansion coefficient and Φ_d is the viscous dissipation function. For simplicity, the gas is assumed to obey the ideal gas law, although the final results can be readily extended to a real gas with suitable modifications. The equation of state is then

$$p = \rho \tilde{R} T, \tag{2.4}$$

with $\tilde{R}$ being the gas constant. For an ideal gas, $\beta T = 1$ in Eq. (2.3).

Petroleum fluid recovery is generally conducted under stepwise small pressure drops in order to maintain the mechanical integrity of the sedimentary rocks. Thus, the pore-scale flow generally falls into the low Mach number and low Reynolds number regime. Therefore, a linearized theory is commonly used. For perturbation of the final equilibrium state $(\mathbf{v}, \rho, T) = (0, \rho_e, T_e)$, which is the state specified at the channel exit (Fig. 1), the linearized continuity and momentum equations for the perturbations are

$$\frac{\partial \rho'}{\partial t} + \rho_e \nabla \cdot \mathbf{v}' = 0, \tag{2.5}$$

$$\rho_e \frac{\partial \mathbf{v}'}{\partial t} = -\nabla p' + (\mu_b + \mu/3)\nabla(\nabla \cdot \mathbf{v}') + \mu \nabla^2 \mathbf{v}', \tag{2.6}$$

where $\rho' = \rho - \rho_e$, $\mathbf{v}' = \mathbf{v}$ are the density and velocity perturbations. Klainerman and Majda [14] have rigorously proved that, for given initial data, the linearized acoustics is a uniformly valid principal correction in the deviation of the compressible flow solution from the incompressible solution as the global Mach number $M \to 0$ [in the present problem, the global Mach number can be conveniently defined as $M = \sqrt{(\rho_i - \rho_e)/\rho_e}$]. This result has been extended by Klein [15] to nonisentropic flows and by Munz *et al.* [16,17] to the general heat conducting viscous compressible Navier-Stokes equations. For drainage flow from a semisealed conduit, the limiting incompressible velocity is identically zero [3,4,5,18]. Then, to the leading order, the velocity is entirely due to the linear acoustic field. From the Helmholtz decomposition theorem [12,19,20], this acoustic velocity

$\mathbf{v}'$, which is induced by compressible effect, can be decomposed into the sum of an irrotational part and a rotational part,

$$\mathbf{v}' = \mathbf{v}'_{IR} + \mathbf{v}'_{RT}, \tag{2.7}$$

where the irrotational part is a potential flow and the rotational part is solenoidal (divergence free):

$$\nabla \times \mathbf{v}'_{IR} = 0, \quad \mathbf{v}'_{IR} = \nabla\Phi, \tag{2.8}$$

$$\nabla \cdot \mathbf{v}'_{RT} = 0. \tag{2.9}$$

In the above, Φ is the scalar velocity potential for the irrotational part of the velocity. A key result from Klainerman and Majda [14] is that the pressure can be decomposed into the sum of a hydrodynamic pressure and a thermodynamic pressure,

$$p' = p'_{hy} + p'_{th}, \tag{2.10}$$

where the hydrodynamic pressure p'_{hy} is a Lagrange multiplier for the incompressible part of the velocity $\mathbf{v}'_{RT}$, and the thermodynamic pressure p'_{th} satisfies the equation of state for an ideal gas, which for the perturbed quantities becomes

$$\frac{p'_{th}}{p_e} = \frac{T'}{T_e} + \frac{\rho'}{\rho_e}, \tag{2.11}$$

where the temperature perturbation $T' = T - T_e$.

After using the vector identity

$$\nabla^2\mathbf{a} = \nabla(\nabla \cdot \mathbf{a}) - \nabla \times (\nabla \times \mathbf{a}), \tag{2.12}$$

the continuity equation and the momentum equations for the two parts of the velocity field become [18]

$$\frac{\partial \rho'}{\partial t} + \rho_e \nabla \cdot \mathbf{v}'_{IR} = 0, \tag{2.13}$$

$$\rho_e \frac{\partial \mathbf{v}'_{IR}}{\partial t} = -\nabla p'_{th} + (\mu_b + 4\mu/3)\nabla^2 \mathbf{v}'_{IR}, \tag{2.14}$$

$$\nabla \cdot \mathbf{v}'_{RT} = 0, \tag{2.15}$$

$$\rho_e \frac{\partial \mathbf{v}'_{RT}}{\partial t} = -\nabla p_{hy}{}' + \mu\nabla^2 \mathbf{v}'_{RT}. \tag{2.16}$$

In the above, we have used the identity

$$\nabla^2 \mathbf{v}'_{IR} = \nabla(\nabla \cdot \mathbf{v}'_{IR}) - \nabla \times (\nabla \times \mathbf{v}'_{IR}) = \nabla(\nabla \cdot \mathbf{v}'_{IR}). \tag{2.17}$$

The pressure in the energy equation (2.3) is the thermodynamic pressure, as the thermal expansion coefficient must come from the thermodynamic pressure. Thus, the linearized energy equation is

$$\rho_e c_p \frac{\partial T'}{\partial t} = \kappa \nabla^2 T' + \frac{\partial p'_{th}}{\partial t}. \tag{2.18}$$

Clearly, in the linearized theory perturbing a state of equilibrium, the governing equations for the field $(\mathbf{v}'_{IR}, p'_{th}, T')$ are decoupled from the equations for the solenoidal field $(\mathbf{v}'_{RT}, p'_{hy})$; the latter is also called the transverse mode in the acoustic literature. The two modes from $(\mathbf{v}'_{IR}, p'_{th}, T')$ are called the longitudinal mode and the thermal (or entropy) mode, respectively. However, the transverse mode is coupled on the boundary to the longitudinal mode and the thermal mode through the no-slip condition for the overall velocity [21]. In fact, in the drainage flow problem considered in

this study, the transverse mode is entirely induced by the longitudinal mode via the no-slip boundary condition.

From Eqs. (2.11), (2.13), (2.14), and (2.18), it can be shown that the density perturbation satisfies the following single equation:

$$\left(\frac{\kappa}{\rho_e\tilde{R}}\frac{\mu_b+4\mu/3}{\rho_e}\frac{\partial}{\partial t}+\frac{\kappa T_e}{\rho_e}\right)\nabla^2\nabla^2\rho'-\left[c_pT_e\frac{\partial}{\partial t}+(c_p/\tilde{R}-1)\frac{\mu_b+4\mu/3}{\rho_e}\frac{\partial^2}{\partial t^2}+\frac{\kappa}{\rho_e\tilde{R}}\frac{\partial^2}{\partial t^2}\right]\nabla^2\rho'$$
$$+(c_p/\tilde{R}-1)\frac{\partial^3\rho'}{\partial t^3}=0. \tag{2.19}$$

Beltman [22] has also derived Eq. (2.19) for the temperature perturbation in the frequency domain. A dimensionless form for Eq. (2.19) is

$$\frac{\partial}{\partial\tilde{t}}\left(\frac{\xi}{\mathrm{Re}}\tilde{\nabla}^2-\frac{\partial}{\partial\tilde{t}}\right)\left(\frac{\gamma}{\mathrm{Pe}}\tilde{\nabla}^2-\frac{\partial}{\partial\tilde{t}}\right)\tilde{\rho}'+\tilde{\nabla}^2\left(\frac{1}{\mathrm{Pe}}\tilde{\nabla}^2-\frac{\partial}{\partial\tilde{t}}\right)\tilde{\rho}'=0, \tag{2.20}$$

where $\gamma=c_p/c_\mathrm{v}$, c_v being the constant-volume specific heat; $\xi=\mu_b/\mu+4/3$, $c=\sqrt{\gamma\tilde{R}T_e}$, $\tilde{\rho}'=\rho'/\rho_e$, $\tilde{\nabla}=L\nabla$, $\tilde{t}=tc/L$; the acoustic Reynolds number $\mathrm{Re}=\rho_ecL/\mu$; the acoustic Péclet number $\mathrm{Pe}=\rho_ec_pcL/\kappa$. L is the length of the channel. The Péclet number $\mathrm{Pe}=\mathrm{Pr}\,\mathrm{Re}$, with $\mathrm{Pr}=\mu c_p/\kappa$ being the Prandtl number. In contrast, when the thermal effect is neglected entirely from the onset (isothermal flow), density change obeys the damped wave equation [3,4,23,24]:

$$\frac{\partial^2\rho'}{\partial t^2}=\left(c^2+\frac{\mu_b+4\mu/3}{\rho_e}\frac{\partial}{\partial t}\right)\nabla^2\rho'. \tag{2.21}$$

Equation (2.20) recovers to the isothermal equation (2.21) in the limit of negligible thermal diffusion when the Péclet number $\mathrm{Pe}\to\infty$.

It is noted that, in order to model the thermal effect without solving the temperature equation, Lighthill [13] has modified the isothermal equation (2.21) to

$$\frac{\partial^2\rho'}{\partial t^2}=\left(c^2+\delta\frac{\partial}{\partial t}\right)\nabla^2\rho', \tag{2.22}$$

with

$$\delta=\delta_\mathrm{v}+\delta_c+\delta_l, \tag{2.23}$$

$$\delta_\mathrm{v}=\frac{4}{3}\frac{\mu}{\rho_e}, \tag{2.24}$$

$$\delta_c=(1-\gamma^{-1})\frac{\kappa}{\rho_ec_\mathrm{v}}=\frac{\gamma-1}{\mathrm{Pr}}, \tag{2.25}$$

$$\delta_l=(\gamma-1)^2\frac{c^2}{\gamma}\sum F_n\tau_n, \tag{2.26}$$

where δ_l results from the nontranslational components of the internal energy (i.e., rotational or vibrational modes), with τ_n being the time lag. Clearly, Lighthill's model equation (2.22) is much simpler than Eq. (2.19), but only the latter has fully considered the thermal effect as it is derived from the full governing equations. Furthermore, Eq. (2.19) is of higher order than Eq. (2.22) in both time and space, reflecting the full coupling between the density and the temperature, both of which are required for a truly nonisothermal flow. The model equation (2.22) does not include the full thermal coupling, as it is of lower order in both time and space. A solution to Eq. (2.19) requires the boundary conditions on the temperature. A solution to Eq. (2.22), however, does not require additional boundary conditions other than the boundary conditions on the density. Crighton [25]

had pointed out that Lighthill's equation (2.22) is appropriate only when the temperature boundary conditions can be ignored.

It can be shown that each of the quantities associated with the longitudinal and thermal modes $(\rho', \mathbf{v}'_{IR}, p'_{th}, T')$ satisfies the same equation (2.19), and they can be solved simultaneously subject to suitable boundary and initial conditions.

III. SOLUTION OF NONISOTHERMAL DRAINAGE FLOW WITH ADIABATIC WALLS

Consider nonisothermal drainage flow from a semisealed channel with adiabatic walls. We first solve the longitudinal and the thermal modes $(\rho', \mathbf{v}'_{IR}, p'_{th}, T')$. For the irrotational velocity, only the no-penetration condition is required on the walls. Thus, the boundary conditions on the channel walls are

$$y = \pm h: \; v'_{IR,y} = 0; \quad \frac{\partial T'}{\partial y} = 0. \tag{3.1}$$

It can be shown that the density and the thermodynamic pressure also satisfy the same Neumann condition on the walls,

$$y = \pm h: \; \frac{\partial \rho'}{\partial y} = \frac{\partial p'_{th}}{\partial y} = 0. \tag{3.2}$$

The boundary conditions in the flow direction are

$$\begin{aligned} x = 0: \; & v'_{IR,x} = 0; \quad \frac{\partial \rho'}{\partial x} = 0; \quad \frac{\partial T'}{\partial x} = 0, \\ x = L: \; & \rho' = 0; \quad T' = 0. \end{aligned} \tag{3.3}$$

In the above, the no-penetration or symmetry condition on the sealed end $x = 0$ is used; at the exit $x = L$, density and temperature are prescribed as $\rho = \rho_e$, $T = T_e$, but the velocity $v'_{IR,x}$ is to be determined from the solutions. The initial conditions are

$$\begin{aligned} t = 0: \; & \rho' = \rho_i - \rho_e, \\ & \frac{\partial \rho'}{\partial t} = 0, \\ & T' = T_i - T_e. \end{aligned} \tag{3.4}$$

Equation (2.19) is solved analytically by the method of separation of variables subject to the boundary and initial conditions for the density. The temperature field is then obtained in terms of the density field and the third initial condition in (3.4) for the temperature is thereafter enforced. The fields $(\rho', \mathbf{v}'_{IR}, p'_{th}, T')$ (longitudinal mode and thermal mode) are then completely determined. The longitudinal mode and the thermal mode turn out to be independent of the transverse coordinate y (plane-wave solution) under the given boundary conditions; they are given by

$$\rho' = \sum_{n=0}^{\infty} \left(\cos \frac{2n+1}{2L} \pi x \right) [B_{n,1} e^{\tilde{\gamma}_{n,1} t} + B_{n,2} e^{\tilde{\gamma}_{n,2} t} + B_{n,3} e^{\tilde{\gamma}_{n,3} t}], \tag{3.5}$$

$$\begin{aligned} p'_{th} = \sum_{n=0}^{\infty} \left(\cos \frac{2n+1}{2L} \pi x \right) \Bigg[& B_{n,1} \left(\frac{\tilde{\gamma}_{n,1}^2}{\alpha_n} - \frac{\mu_b + 4\mu/3}{\rho_e} \tilde{\gamma}_{n,1} \right) e^{\tilde{\gamma}_{n,1} t} \\ & + B_{n,2} \left(\frac{\tilde{\gamma}_{n,2}^2}{\alpha_n} - \frac{\mu_b + 4\mu/3}{\rho_e} \tilde{\gamma}_{n,2} \right) e^{\tilde{\gamma}_{n,2} t} + B_{n,3} \left(\frac{\tilde{\gamma}_{n,3}^2}{\alpha_n} - \frac{\mu_b + 4\mu/3}{\rho_e} \tilde{\gamma}_{n,3} \right) e^{\tilde{\gamma}_{n,3} t} \Bigg], \end{aligned} \tag{3.6}$$

$$T' = \sum_{n=0}^{\infty}\left(\cos\frac{2n+1}{2L}\pi x\right)\left\{B_{n,1}\left[\frac{T_e}{p_e}\left(\frac{\tilde{\gamma}_{n,1}^2}{\alpha_n} - \frac{\mu_b + 4\mu/3}{\rho_e}\tilde{\gamma}_{n,1}\right) - \frac{T_e}{\rho_e}\right]e^{\tilde{\gamma}_{n,1}t}\right.$$
$$+ B_{n,2}\left[\frac{T_e}{p_e}\left(\frac{\tilde{\gamma}_{n,2}^2}{\alpha_n} - \frac{\mu_b + 4\mu/3}{\rho_e}\tilde{\gamma}_{n,2}\right) - \frac{T_e}{\rho_e}\right]e^{\tilde{\gamma}_{n,2}t}$$
$$\left. + B_{n,3}\left[\frac{T_e}{p_e}\left(\frac{\tilde{\gamma}_{n,3}^2}{\alpha_n} - \frac{\mu_b + 4\mu/3}{\rho_e}\tilde{\gamma}_{n,3}\right) - \frac{T_e}{\rho_e}\right]e^{\tilde{\gamma}_{n,3}t}\right\}, \tag{3.7}$$

$$\mathrm{v}'_{IR,x} = \sum_{n=0}^{\infty}\frac{2n+1}{2L}\pi\left(\sin\frac{2n+1}{2L}\pi x\right)\frac{1}{\rho_e\alpha_n}(B_{n,1}\tilde{\gamma}_{n,1}e^{\tilde{\gamma}_{n,1}t} + B_{n,2}\tilde{\gamma}_{n,2}e^{\tilde{\gamma}_{n,2}t} + B_{n,3}\tilde{\gamma}_{n,3}e^{\tilde{\gamma}_{n,3}t}), \tag{3.8}$$

$$\mathrm{v}'_{IR,y} = 0, \tag{3.9}$$

where $T_e/p_e = 1/(\rho_e\tilde{R})$,

$$\alpha_n = -\left(\frac{2n+1}{2L}\pi\right)^2, \quad n = 0, 1, 2, 3\cdots, \tag{3.10}$$

and $\tilde{\gamma}_{n,1}$, $\tilde{\gamma}_{n,2}, \tilde{\gamma}_{n,3}$ are the roots of the cubic equation

$$a_n\tilde{\gamma}^3 + b_n\tilde{\gamma}^2 + c_n\tilde{\gamma} + d_n = 0, \tag{3.11}$$

with

$$a_n = \frac{c_p}{\tilde{R}} - 1, \tag{3.12}$$

$$b_n = -\left[\alpha_n\left(\frac{c_p}{\tilde{R}} - 1\right)\frac{\mu_b + 4\mu/3}{\rho_e} + \alpha_n\frac{\kappa}{\rho_e\tilde{R}}\right], \tag{3.13}$$

$$c_n = \alpha_n^2\frac{\kappa}{\rho_e\tilde{R}}\frac{\mu_b + 4\mu/3}{\rho_e} - \alpha_n c_p T_e \tag{3.14}$$

$$d_n = \alpha_n^2\frac{\kappa T_e}{\rho_e}. \tag{3.15}$$

It is noted that the pair $\tilde{\gamma}_2$, $\tilde{\gamma}_3$ are complex conjugates and they correspond to the oscillatory motion of the damped waves, while $\tilde{\gamma}_1$ is real and negative (purely diffusive and associated with thermal diffusion). The coefficients $B_{n,1}$, $B_{n,2}$, $B_{n,3}$ are listed in Appendix A.

The solenoidal field (transverse mode) ($\mathbf{v}'_{RT}$, p'_{hy}) are induced by the irrotational field via the no-slip condition for the overall velocity on the walls,

$$y = \pm h: \ \mathbf{v}' = \mathbf{v}'_{IR} + \mathbf{v}'_{RT} = 0, \tag{3.16}$$

and they are obtained numerically. For drainage from a semisealed channel, however, the solenoidal velocity $\mathbf{v}'_{RT}$ does not contribute to the mass flux, as integration of the solenoidality condition $\nabla \cdot \mathbf{v}'_{RT} = 0$ over the entire domain leads to the corresponding volumetric flow rate,

$$Q_{RT}(x) = \int_{\text{Cross section}} \mathbf{n}\cdot\mathbf{v}'_{RT}da = 0, \tag{3.17}$$

since the end at $x = 0$ is sealed. The solenoidal field is two dimensional and an example of the solenoidal solution is shown in Appendix B.

The analytical solution to the longitudinal and thermal modes is validated by the numerical solution of the initial-boundary-value problem (IBVP) for the corresponding system of linear equations. After a simple manipulation to yield a coupled system in terms of only the perturbed

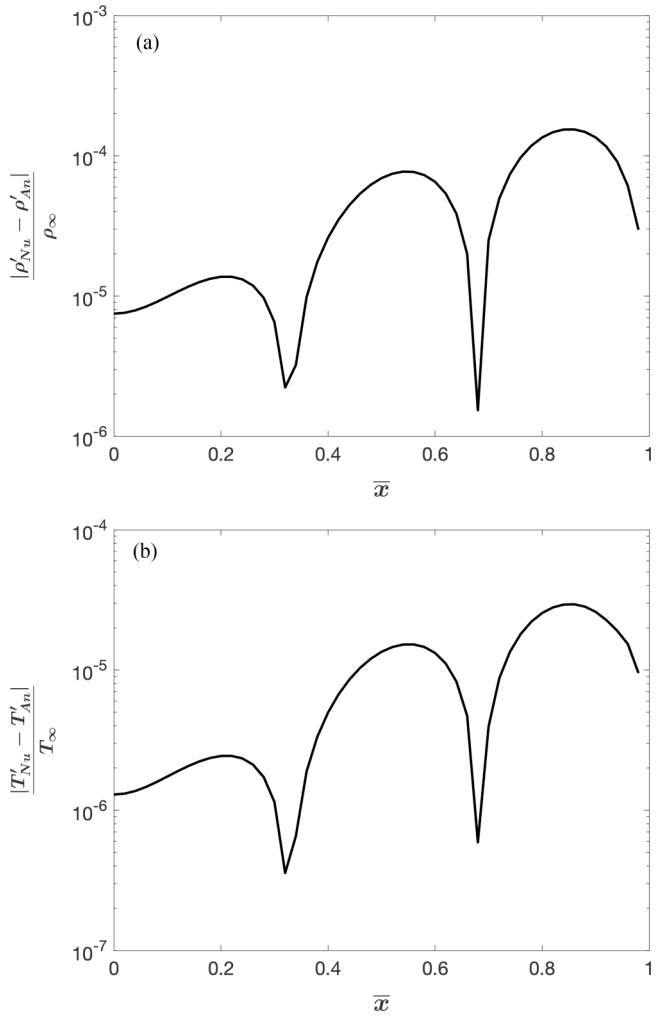

FIG. 2. The difference between the analytical solution and the numerical solution at the end of one period for ethylene. $\rho_e = 52.15\,\mathrm{kg/m^3}$, $T_e = 375\,\mathrm{K}$, $\rho_i/\rho_e = 1.02$, $T_i/T_e = 1.02$. (a) Normalized excess density in the channel; (b) normalized excess temperature in the channel.

temperature T' and the perturbed density ρ', the IBVP is then solved numerically using the built-in partial differential equation package CFPDE in COMSOL [26]. In all numerical calculations reported in this study, the time step used is $1/1024$ of the period of the acoustic wave oscillation, $4L/c$, which ensures full and accurate resolution of the acoustic oscillation. Convergence tests have been conducted by increasing the number of elements used. When using the analytical solution, care is taken to ensure that enough terms are retained in the infinite series to give a convergent result. For the purpose of comparison, ethylene is used as the gas, with its physical property listed in Table I in Appendix C. The microchannel has a gap 200 nm, length 10 μm; and $\rho_e = 52.15\,\mathrm{kg/m^3}$, $T_e = 375\,\mathrm{K}$, and $\rho_i/\rho_e = 1.02$, $T_i/T_e = 1.02$. The period of oscillation is 1.095×10^{-7} s. In the text below, we have designated the final equilibrium state (ρ_e, T_e) as (ρ_∞, T_∞). The normalized excess density ρ'/ρ_∞ in the channel from the analytical solution is compared to the numerically computed values for the first oscillatory period. Figure 2(a) shows the differences of the analytically obtained and the numerically computed normalized excess density ρ'/ρ_∞ at the end of the period for the entire channel. The differences are no more than 2×10^{-4}. A similarly satisfactory comparison is

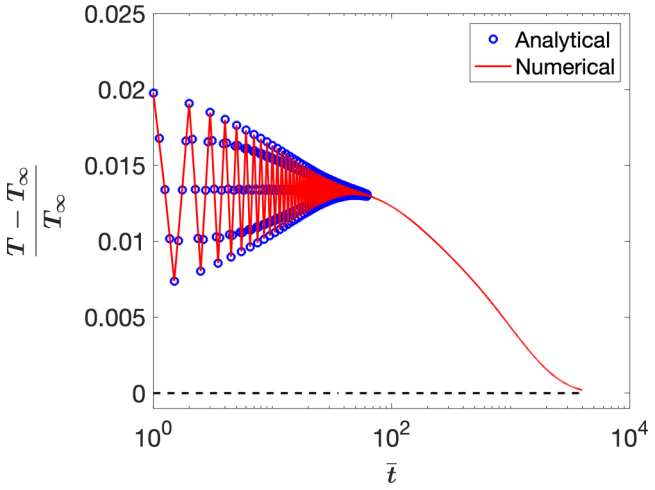

FIG. 3. Normalized excess temperature at the midchannel location $x = L/2$ as a function of time normalized by the oscillation period for ethylene. $\rho_e = 52.15\,\mathrm{kg/m^3}$, $T_e = 375\,\mathrm{K}$, $\rho_i/\rho_e = 1.02$, $T_i/T_e = 1.02$. The analytical solution captures the oscillation and it agrees very well with the numerical solution.

achieved for the normalized excess temperature T'/T_∞ in the channel: Figure 2(b) shows that the analytical solution and the numerical solution for the normalized excess temperature differ less than 3×10^{-5}. Figure 3 shows the normalized excess temperature at the midchannel $x = L/2$ for longer times, where $\bar{t}$ is the time normalized by the oscillation period. The analytical solution accurately captures the oscillations and it agrees very well with the numerical solution.

The excess mass inside the channel is the difference between the instantaneous mass and the final equilibrium mass, $m(t) - m_\infty$, with $m_\infty = 2\rho_e hL$. Figure 4 shows the normalized excess mass $(m - m_\infty)/m_\infty$ inside the channel as a function of the normalized time $\bar{t}$. Clearly, the analytical solution resolves the short time oscillations and it agrees with the numerical solution. From Fig. 4, it is also observed that the excess mass not only oscillates in time, but also can become negative, indicating that the density inside the tube can actually drop below the exit density. It will be shown

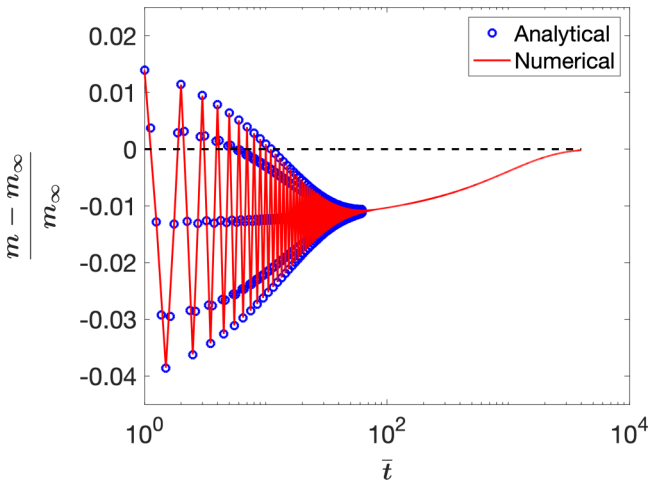

FIG. 4. Excess mass inside the channel plotted for long times for ethylene. $\rho_e = 52.15\,\mathrm{kg/m^3}$, $T_e = 375\,\mathrm{K}$, $\rho_i/\rho_e = 1.02$, $T_i/T_e = 1.02$. Negative value implies that the mass in the channel is below the final equilibrium value and fluid will be drawn from the reservoir into the channel.

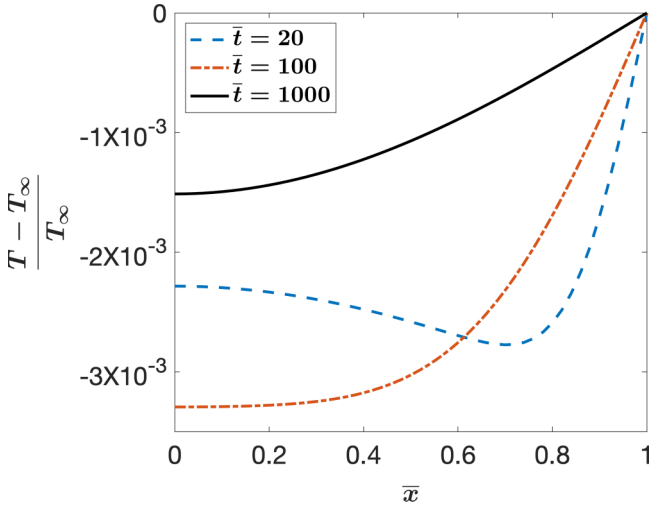

FIG. 5. Transient temperature distribution inside the channel for ethylene for the nonisothermal model with $\rho_i/\rho_e = 1.02$, $\rho_e = 52.15\,\mathrm{kg/m^3}$, $T_i = T_e = T_\infty$ at instants $\bar{t} = 20,\ 100,\ 1000$. Temperature deceases from the initial condition $T = T_i$ first; it then recovers at larger times, and eventually returns to $T = T_i$. Temperature stays above the final equilibrium temperature at all times.

later that the excess mass can even stay negative for a prolonged period of time due to thermal effects.

IV. THERMAL EFFECT ON THE MASS DRAINAGE RATE

Since the channel is semisealed and the solution for the density is independent of the transverse coordinate y for adiabatic walls (plane-wave solution), integration of the continuity equation (2.1) over the volume of the entire channel gives the mass flow rate at the channel exit (drainage rate) as

$$\dot{m}_e = -\int_{\text{channel}} \frac{\partial \rho}{\partial t} dV = -A \frac{\partial}{\partial t} \int_{\text{length}} \rho dx, \tag{4.1}$$

where A is the cross-sectional area of the channel. Equation (4.1) indicates that the mass flow rate is linearly proportional to the channel height. Therefore, the mass flow rate is sliplike, even though the overall velocity, $\mathbf{v}' = \mathbf{v}'_{IR} + \mathbf{v}'_{RT}$, satisfies the no-slip condition on the channel walls.

The thermal effect on the fluid recovery process can be examined by comparing the instantaneous excess mass inside the channel for the present nonisothermal model to that of the isothermal model with the same density drop $\Delta\rho = \rho_i - \rho_\infty$. We first consider the case of zero imposed temperature change, $T_i = T_e$. The classical approach would have argued that such a flow is isothermal with uniform temperature inside the channel, justifying the use of the isothermal model. However, if we use the full nonisothermal equation (2.19), there are nonzero transient temperature variations inside the channel even for $T_i = T_e$. An example of this is shown in Fig. 5 for ethylene with $\rho_e = 52.15\,\mathrm{kg/m^3}$, $T_e = 375\,\mathrm{K}$, $\rho_i/\rho_e = 1.02$, $T_i = T_e$ for the time instants $\bar{t} = 20,\ 100,\ 1000$. The temperature is initially uniform inside the channel, $T = T_i$. Once the motion commences, the temperature dips below T_i everywhere due to the expansion of the gas and it continues to drop in time, such as at $\bar{t} = 20$ and $\bar{t} = 100$. The temperature then begins to recover at larger times (e.g., $\bar{t} = 1000$) and it eventually recovers back to $T = T_i$. This nontrivial behavior for the case of zero imposed temperature drop $T_i = T_e$ can be inferred from the temperature equation (2.18): after the

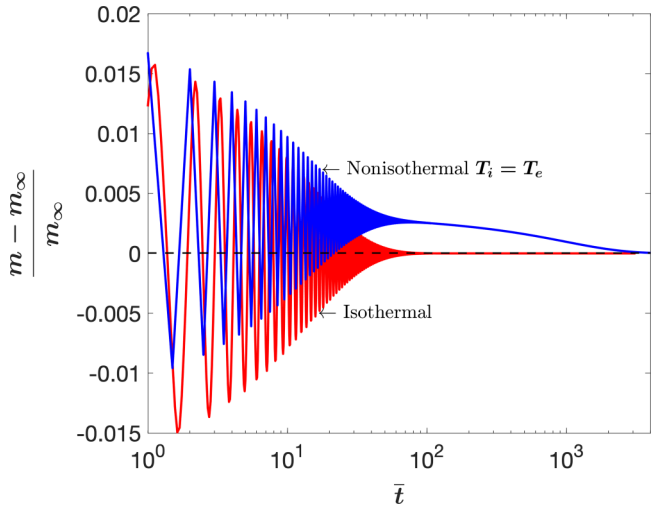

FIG. 6. Comparison of excess mass between isothermal model and nonisothermal model with $T_i = T_e$ for ethylene. For both cases, $\rho_i/\rho_e = 1.02$, $\rho_e = 52.15\,\mathrm{kg/m^3}$.

pressure time derivative term is eliminated by using Eq. (2.11), Eq. (2.18) becomes

$$\frac{\rho_e \tilde{R}}{\gamma - 1}\frac{\partial T'}{\partial t} = \kappa \nabla^2 T' + \tilde{R} T_e \frac{\partial \rho'}{\partial t}. \tag{4.2}$$

Thus, even when $T_i = T_e$, the time rate of change in the density [the last term on the right-hand side of Eq. (4.2)] can cause a nonzero transient temperature change inside the channel. Such a result is completely absent in an incompressible flow or when a low Mach number compressible flow is approximated as an incompressible flow. The nontrivial solution is also evident from the

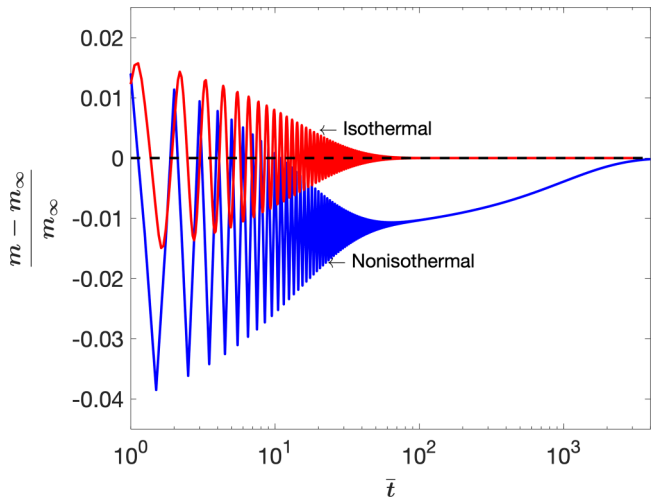

FIG. 7. Excess mass inside the channel for draiange of ethelyne for the isothermal model and the present nonisothermal model. $\rho_i/\rho_e = 1.02$, $\rho_e = 52.15\,\mathrm{kg/m^3}$. For the nonisothermal model, $T_e = 375\,\mathrm{K}$, $T_i/T_e = 1.02$. When $\bar{t} > 10$, the excess mass stays negative, indicating an undershoot of the mass below the final equilibrium mass.

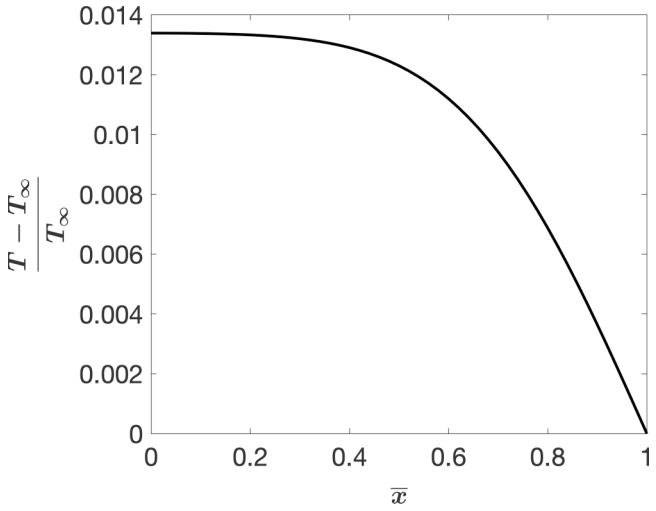

FIG. 8. Excess temperature distribution at $\bar{t} = 100$ when oscillations in the density disappear for the nonisothermal case of $\rho_i/\rho_e = 1.02$, $\rho_e = 52.15\,\mathrm{kg/m^3}$, $T_e = 375\,\mathrm{K}$,$T_i/T_e = 1.02$. The temperature inside the channel is everywhere above the exit temperature.

analytical solution for T', Eq. (3.7): When $T_i = T_e$, the coefficients for the three time-exponential terms $e^{\tilde{\gamma}_{n,i}t}(i = 1, 2, 3)$ do not vanish.

Figure 6 compares the excess mass for the nonisothermal model with $T_i = T_e$ and the isothermal model. The gas expansion induced transient drop in temperature hinders the drainage process, as it takes longer for the mass inside the channel to drop to the final equilibrium value when compared to the isothermal model. Clearly, setting $T_i = T_e$ does not give rise to the isothermal model as one would have expected for an incompressible fluid [for which the last term on the right-hand side

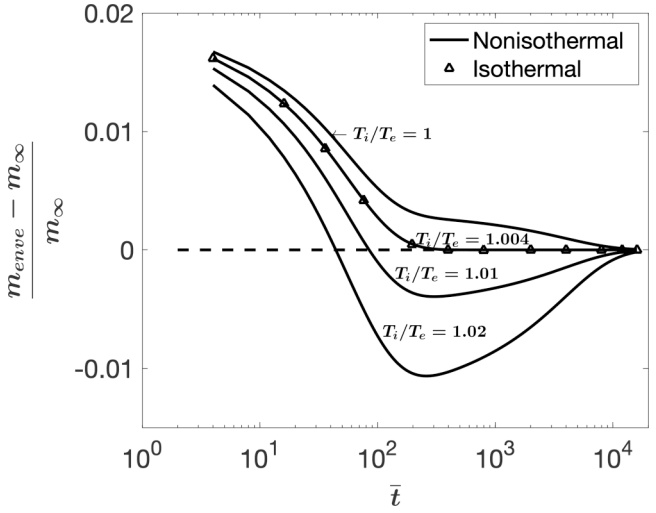

FIG. 9. The envelope of the excess mass inside the channel for ethylene for the isothermal model and the nonisothermal model. $T_e = 375\,\mathrm{K}$, $\rho_e = 52.15\,\mathrm{kg/m^3}$, $\rho_i/\rho_e = 1.02$. The nonisothermal model with $T_i/T_e = 1.004$ coincides with the isothermal case. The excess mass from the nonisothermal model undershoots the final equlibrium value when $T_i/T_e > 1.004$.

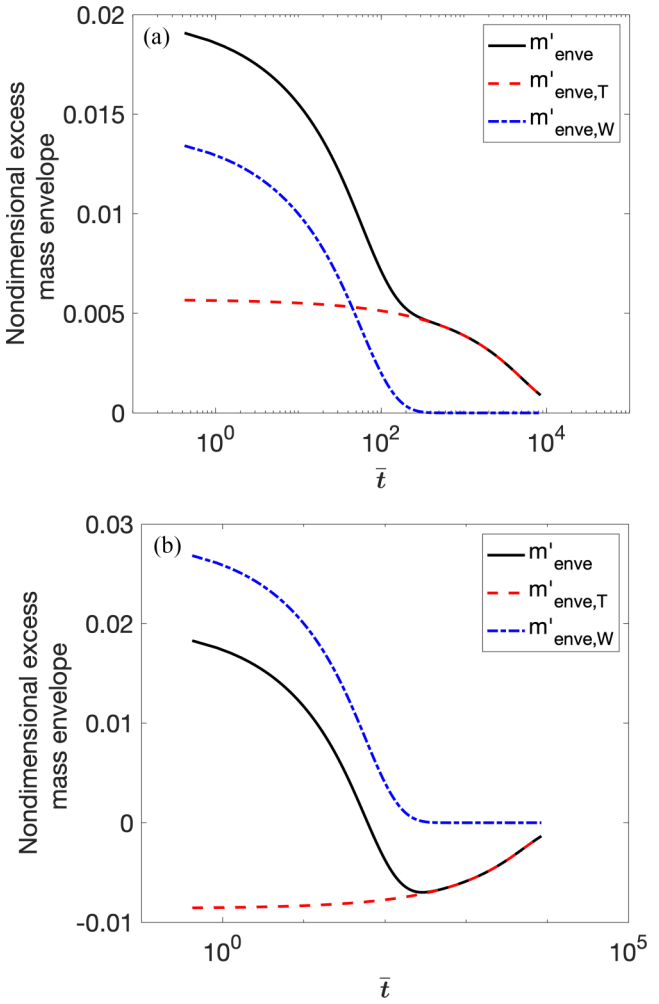

FIG. 10. Envelope of the excess mass for ethylene for the nonisothermal model with $T_e = 375\,\mathrm{K}$, $\rho_e = 52.15\,\mathrm{kg/m^3}$, $\rho_i/\rho_e = 1.02$. (a) No imposed temperature drop, $T_i/T_e = 1$. (b) Imposed temperature drop $T_i/T_e = 1.02$. The thermal energy diffusion contribution to the envelope $m'_{\mathrm{enve},T}$ is always positive for (a) but always negative for (b), indicating hindrance and enhancement of the drainage process by thermal energy diffusion effect, respectively.

of Eq. (4.2) vanishes] or from a traditional scaling analysis. The isothermal flow solution for a compressible gas is only achievable when thermal energy diffusion is negligible, or in the limit of the Péclet number $\mathrm{Pe} \to \infty$, as discussed in Sec. II.

For nonisothermal flows, there are two independent state variables such as ρ, T. For fixed ρ_i, ρ_e, when T_i/T_e is increased past unity, the thermal energy diffusion effect can enhance the drainage process when T_i/T_e is large enough. For example, for $\rho_i/\rho_e = 1.02$, $T_i/T_e = 1.02$, $\rho_e = 52.15\,\mathrm{kg/m^3}$, $T_e = 375\,\mathrm{K}$, Fig. 7 shows the normalized excess mass inside the channel as a function of the normalized time for the isothermal and the nonisothermal drianage flows. For isothermal drianage, the excess mass oscilates symmetrically about the final equilibrium value (zero) with a time-decaying amplitude. Each period of oscillation produces a small amount of fluid due to the ampltiude decay. For the nonisothermal drianage model, the oscillation in the mass becomes asymmetrical about the final equilibrium value; the magnitude of oscillation is greater than that

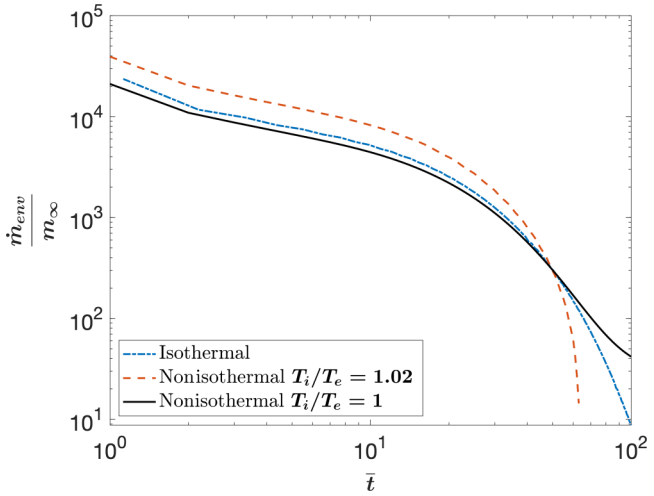

FIG. 11. Mass flow rates for ethylene for the isothermal model and the nonisothermal model with $T_i/T_e = 1$ and $T_i/T_e = 1.02$. $\rho_i/\rho_e = 1.02$. The noniosthermal model can give a mass flow rate either higher or lower than that for the iosthermal model depending on the magnitude of T_i/T_e.

for the isothermal model. As time progresses, the excess mass for the nonisothermal driange flow becomes and stays negative during the entire oscillation period at large times, indicating that the denisty inside the channel has fallen below and remains below the exit density. This shows that the thermal effect significantly speeds up the drainage process and it leads to an undershoot of the density below the final equilibrium denisty when $T_i/T_e = 1.02$. However, there is no undershoot of the temperature (see Fig. 3). The oscillations in the excess mass for both models, however, disappear at the same time instant, roughly after 100 cycles. For the isothermal model, the final equilibrium state is reached at this time instant, while for the nonisothermal model, it has to recover from the undershoot of the final equilibrium. This recovery process is nonoscillatory and dominated by thermal energy diffusion, which eventually brings the excess mass from negative values to the final equilibrium value of zero. During this final nonoscillatory period, the density inside the channel stays below the final equilibrium value, while the temperature stays above the final equilibrium temperature (Fig. 8). This final nonoscillatory portion of the process is to draw fluid from the outside back into the channel, because the density inside the channel is below the exit density and the temperature is higher than the exit temperature.

Another way to characterize the drainage process is to plot the excess mass at the end of each oscillation period, which corresponds to the envelope of the excess mass curves in Figs. 6 and 7. The envelopes, shown in Fig. 9 for the isothermal and nonisothermal models with $T_i/T_e = 1.0,\ 1.004,\ 1.01,\ 1.02$, all with $\rho_i/\rho_e = 1.02$, $T_e = 375$ K, allow us to ignore the details of acoustic oscillations and focus on the mass change over a large time scale. The nonisothermal model with $T_i/T_e = 1.004$ coincides with the isothermal case. For a small imposed temperature change in the range $1 \leqslant T_i/T_e < 1.004$, the isothermal flow drains faster. For nonisothermal flow with $T_i/T_e > 1.004$, the excess mass is reduced to zero more quickly and it goes on to undershoot the final equilibrium value (zero) by staying in the negative territory before it recovers to zero. Thus, compared to isothermal draiange, the thermal effect accelerates the drainage process for a larger temperature drop, $T_i/T_e > 1.004$, as the excess mass is brought to zero quickly before the undershoot. It is interesting to observe that the final equilibrium state is reached at the same time instant for all nonisothermal cases $T_i/T_e \geqslant 1$.

Further insights can be gained by analyzing the envelope equation for the excess mass, which is derived by integrating the analytical solution for the excess density equation (3.5) over the volume

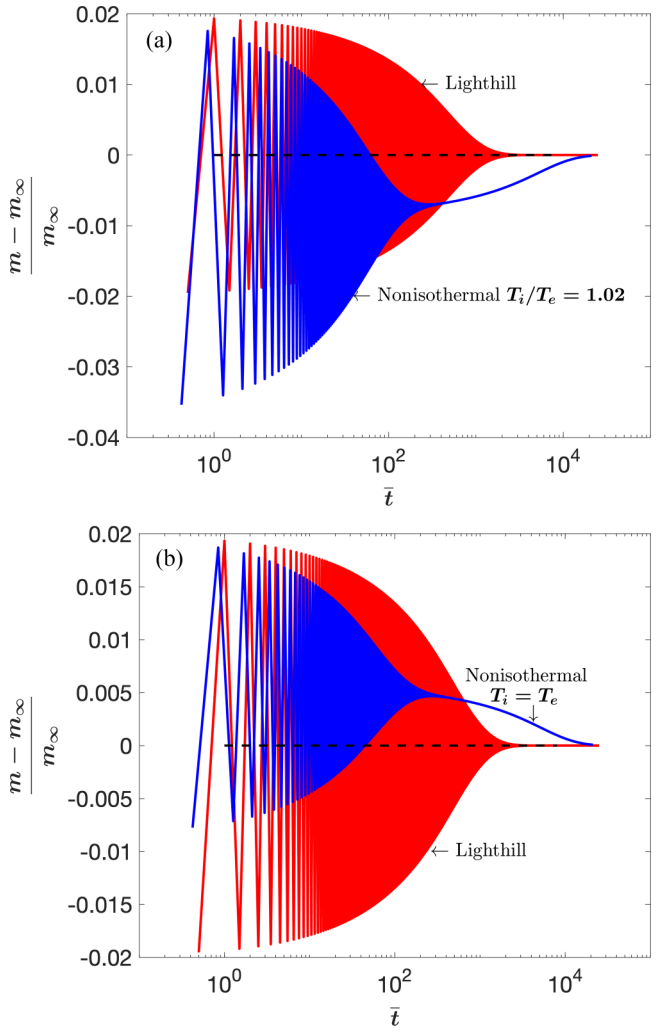

FIG. 12. Comparison of the excess mass inside the channel between Lighthill's model and the nonisothermal model with different T_i/T_e for nitrogen. (a) $T_i/T_e = 1.02$; (b) $T_i/T_e = 1$.

of the channel and then evaluated at the end of each period,

$$m'_{\text{enve}} = \sum_{n=0}^{\infty} \frac{2(-1)^n LH}{(2n+1)\pi} [B_{n,1} e^{\tilde{\gamma}_{n,1} t} + 2\text{Re}(B_{n,2}) e^{\text{Re}(\tilde{\gamma}_{n,2}) t}], \tag{4.3}$$

where Re stands for the real part. This envelope solution is validated by the numerical solution using COMSOL. As we commented previously, $\tilde{\gamma}_{n,1}$ is real and negative, corresponding to thermal energy diffusion, while $\text{Re}(\tilde{\gamma}_{n,2})$ is negative and it corresponds to the damping rate of the acoustic waves. Thus, the envelope equation for the excess mass can be expressed as

$$m'_{\text{enve}} = m'_{\text{enve},T} + m'_{\text{enve},W}, \tag{4.4}$$

with $m'_{\text{enve},T}$, $m'_{\text{enve},W}$ corresponding to the contributions from the thermal energy diffusion and the acoustic wave, respectively. Figure 10 shows m'_{enve}, $m'_{\text{enve},T}$, and $m'_{\text{enve},W}$ for the case of zero imposed temperature drop $T_i/T_e = 1$ and the case of nonzero imposed temperature drop $T_i/T_e = 1.02$. When

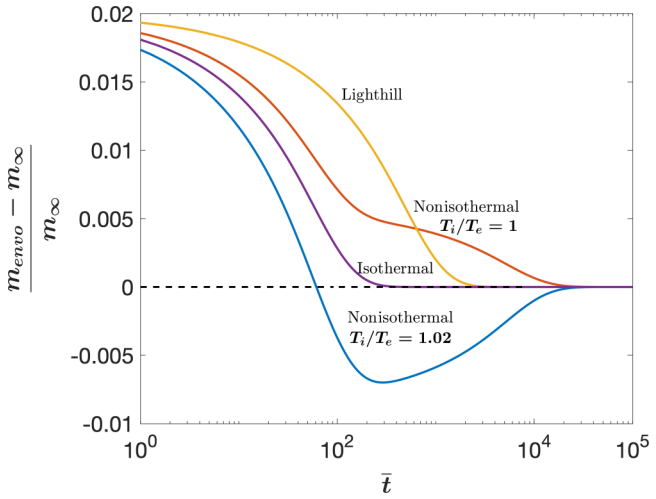

FIG. 13. Comparison of the envelope for the excess mass for the isothermal model, Lighthill's model, and the nonisothermal model with $T_i/T_e = 1.0,\ 1.02$ for nitrogen.

no temperature drop is imposed, the thermal energy diffusion contribution to the excess envelope $m'_{\text{enve},T}$ is always positive [Fig. 10(a)]. This indicates that thermal energy diffusion slows down the decay of the excess mass, retarding the drainage process. This observation supports our earlier conclusion that in the absence of an imposed temperature drop, the gas expansion induced transient drop in temperature hinders the drainage process (Fig. 6). On the other hand, for an imposed temperature drop of $T_i/T_e = 1.02$, the thermal energy contribution $m'_{\text{enve},T}$ is always negative [Fig. 10(b)], confirming that for a large imposed temperture drop, the thermal effect reduces the excess mass and speeds up the drainage process (Fig. 7).

By taking the time derivative of the envelope equation for the mass inside the channel, we can obtain the net mass flow rate over each period at the exit of the channel. This period-averaged mass flow rate is plotted in Fig. 11 on a log-log scale for the isothermal case and the nonisothermal cases with $T_i/T_e = 1$ and $T_i/T_e = 1.02$. It is observed that the mass flow rate obeys the negative one-half power law in the early times for the isothermal as well as the nonisothermal drainage flows, followed by an accelerated exponential drop-off to zero. Except for the final exponential decay, the mass flow rate for nonisothermal drainage with $T_i/T_e = 1.02$ is much greater than that for the isothermal drainage. This fast drainage leads to a much shorter drain-out time for the nonisothermal drainage, since the amount of producible fluid, solely determined by the density drop, is the same for all cases. These results show that neglecting the thermal effect can lead to a significant underestimation of the production rate. The opposite is true for the nonisothermal case with $T_i/T_e < 1.004$.

V. COMPARISON WITH LIGHTHILL'S MODEL EQUATION

The solution to the nonisothermal drainage flow is also compared to the corresponding solution to Lighthill's model equation (2.22). To this end, nitrogen is used (Table II, Appendix C). For nitrogen, only $n = 1$ is retained in δ_l [Eq. (2.26)]; and $\tau_1 = 0.9\,\text{ns} = 0.9 \times 10^{-9}$ s and $F_n = 1$ [13]. The analytical solution of Eq. (2.22) subject to the same boundary and initial conditions for the density as Eq. (2.19) is

$$\rho'(r, x, t) = \frac{4(\rho_i - \rho_e)}{\pi} \sum_{n=0}^{N_d} \frac{(-1)^n}{2n+1} e^{-\gamma_n t} \cos(\omega_n t) \cos\frac{(2n+1)\pi x}{2L}, \tag{5.1}$$

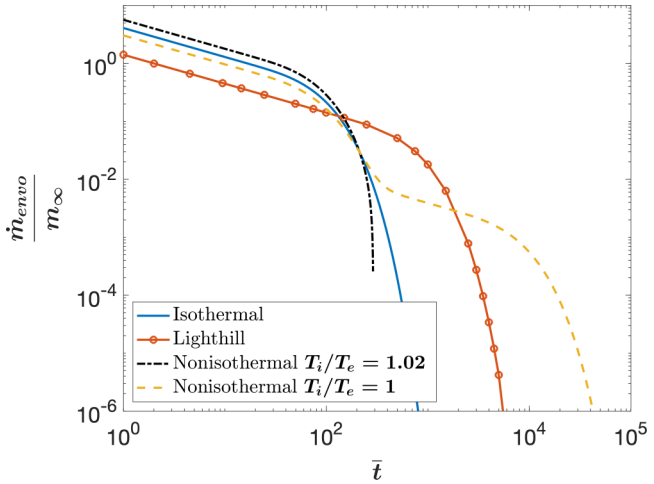

FIG. 14. The mass flow rate curves corresponding to Fig. 12.

$$\sigma_n = \frac{(2n+1)\pi}{2L}; \quad \gamma_n = \frac{\delta}{2}\sigma_n^2; \quad \omega_n = c\sigma_n\sqrt{1 - \frac{\delta^2\sigma_n^2}{4c^2}} \approx c\sigma_n, \tag{5.2}$$

$$N_d = \text{floor}\left[\frac{2cL}{\pi\delta} - \frac{1}{2}\right], \tag{5.3}$$

where the speed of sound is $c = \sqrt{\tilde{R}T_e}$ for isothermal flow; and the floor function gives the maximum integer less than or equal to its argument. The channel has a length of 0.1 mm and gap 2 μm.

Figure 12 compares the excess mass computed from Lighthill's model equation with those from the full equation (2.19) for $T_i/T_e = 1.0,\ 1.02$ for nitrogen. Lighthill's model equation gives an oscillatory excess mass symmetrical about zero, similar to that given by the isothermal damped wave equation (2.21). The nonisothermal model with $T_i/T_e = 1.02$ drains to zero faster than Lighthill's (before the undershoot), while the nonisothermal model with $T_i/T_e = 1$ drains slower than Lighthill's.

In Fig. 13, we plot the envelopes of the excess mass for nitrogen for isothermal [i.e., the damped wave equation (2.21)], nonisothermal, and Lighthill's equations. The nonisothermal model with $T_i/T_e = 1.02$ has the shortest drain-out time (excluding the undershoot and recovery), while the isothermal model and Lighthill's equation have the second and third shortest drain-out time, respectively. The nonisothermal case with $T_i/T_e = 1$ always has the longest drain-out time. The reason that Lighthill's equation underperforms compared to the isothermal equation is that the bulk viscosity contribution to the diffusion coefficient is included through the time-lag term δ_l in the diffusion coefficient, which for nitrogen provides a smaller overall diffusion coefficient compared to the isothermal equation with the diffusion coefficient computed directly using the bulk viscosity value.

The corresponding mass flow rate comparisons are shown in Fig. 14. All the mass flow rate curves obey the negative one-half power law initially before a rapid exponential drop. The nonisothermal case with $T_i/T_e = 1.02$ has the highest mass flow rate before a rapid descent as the excess mass undershoots zero. For smaller temperature drops, the performance of the nonisothermal cases may fall below the isothermal case, even below that from Lighthill's equation.

VI. CONCLUSIONS

This study shows that volumetric-expansion-driven drainage flow of a viscous gas from a semisealed narrow channel with adiabatic walls is strongly influenced by the thermal diffusion effect. Even when the temperature at the exit is not lowered, there is still a transient temperature drop inside the channel due to gas expansion. The commonly adopted isothermal assumption can only be achieved in the limit of infinite Péclet number. For a given density drop, the drain-out time predicted from the isothermal equation or Lighthill's equation is shorter than the nonisothermal case for small temperature ratio T_i/T_e, but longer than the nonisothermal case for large T_i/T_e. Therefore, thermal effect must be taken into consideration for accurate prediction of the drainage process.

APPENDIX A: COEFFICIENTS $B_{n,1}$, $B_{n,2}$, $B_{n,3}$

$$B_{n,1} = -\frac{\left(-X_{n,3}\tilde{\gamma}_2 + X_{n,2}\tilde{\gamma}_3\right)\frac{4(\rho_i-\rho_e)}{\pi}\frac{(-1)^n}{2n+1} + (\tilde{\gamma}_2 - \tilde{\gamma}_3)\frac{4(T_i-T_e)}{\pi}\frac{(-1)^n}{2n+1}}{X_{n,2}\tilde{\gamma}_1 - X_{n,3}\tilde{\gamma}_1 - X_{n,1}\tilde{\gamma}_2 + X_{n,3}\tilde{\gamma}_2 + X_{n,1}\tilde{\gamma}_3 - X_{n,2}\tilde{\gamma}_3}, \tag{A1}$$

$$B_{n,2} = -\frac{(X_{n,3}\tilde{\gamma}_1 - X_{n,1}\tilde{\gamma}_3)\frac{4(\rho_i-\rho_e)}{\pi}\frac{(-1)^n}{2n+1} + (-\tilde{\gamma}_1 + \tilde{\gamma}_3)\frac{4(T_i-T_e)}{\pi}\frac{(-1)^n}{2n+1}}{X_{n,2}\tilde{\gamma}_1 - X_{n,3}\tilde{\gamma}_1 - X_{n,1}\tilde{\gamma}_2 + X_{n,3}\tilde{\gamma}_2 + X_{n,1}\tilde{\gamma}_3 - X_{n,2}\tilde{\gamma}_3}, \tag{A2}$$

$$B_{n,3} = -\frac{(-X_{n,2}\tilde{\gamma}_1 + X_{n,1}\tilde{\gamma}_2)\frac{4(\rho_i-\rho_e)}{\pi}\frac{(-1)^n}{2n+1} + (\tilde{\gamma}_1 - \tilde{\gamma}_2)\frac{4(T_i-T_e)}{\pi}\frac{(-1)^n}{2n+1}}{X_{n,2}\tilde{\gamma}_1 - X_{n,3}\tilde{\gamma}_1 - X_{n,1}\tilde{\gamma}_2 + X_{n,3}\tilde{\gamma}_2 + X_{n,1}\tilde{\gamma}_3 - X_{n,2}\tilde{\gamma}_3}. \tag{A3}$$

It is noted that $B_{n,1}$ is real, while $B_{n,2}$ and $B_{n,3}$ are complex conjugate as shown before.

$$X_{n,i} = \frac{1}{\rho_e\tilde{R}}\left(\frac{\tilde{\gamma}_i^2}{\alpha_n} - \frac{\mu_b + 4\mu/3}{\rho_e}\tilde{\gamma}_i\right) - \frac{T_e}{\rho_e}, \quad (i = 1, 2, 3). \tag{A4}$$

APPENDIX B: SOLUTION FOR THE SOLENOIDAL MODE

The solenoidal velocity field is governed by the incompressible equations (2.15) and (2.16). The solenoidal velocity field is driven by the irrotational field on the channel wall via the no-slip condition, $\mathbf{v}_{IR} + \mathbf{v}_{RT} = 0$. As shown by Chen and Shen [3,4], for drainage flows, the solenoidal field does not generate any mass flow rate and its role is to enforce the no-slip condition for the overall velocity. At the exit ($x = L$), the perturbation of the pressure for the solenoidal velocity field is zero. At the left boundary ($x = 0$), the irrotational velocity is zero, $\mathbf{v}_{IR} = 0$. A numerical approach is adopted in calculating the solenoidal field, as an analytical solution for the solenoidal field is difficult to obtain, even when the irrotational velocity field is a plane-wave solution. The software package COMSOL [26] is used for the calculations. The PARDISO direct solver is employed, with the above boundary conditions. The generalized alpha time stepping method is used with maximum time step: 17sol;500 of the oscillation period. Quad elements are set up in the entire computing domain by using a mapped mesh tool. The height of each mesh element is 1/8 of the half height of the channel. The width of the mesh is 1/512 of the channel length (in our computational example for ethylene below, $h/L = 1/100$, Appendix C, Table I). As mentioned in Eqs. (3.55) and (3.56), the two eigenvalues γ_2 and γ_3 are complex conjugate which make the solution oscillatory in time. Figures 15(a)–15(h) show the solenoidal velocity field in each 1/8 period, where the period $T = 1.094 \times 10^{-7}$ s. The velocity magnitude becomes quite small at the time of half period and then the velocity vector reverses its direction.

APPENDIX C: GAS PROPERTIES

See Tables I and II for gas properties used in the calculations.

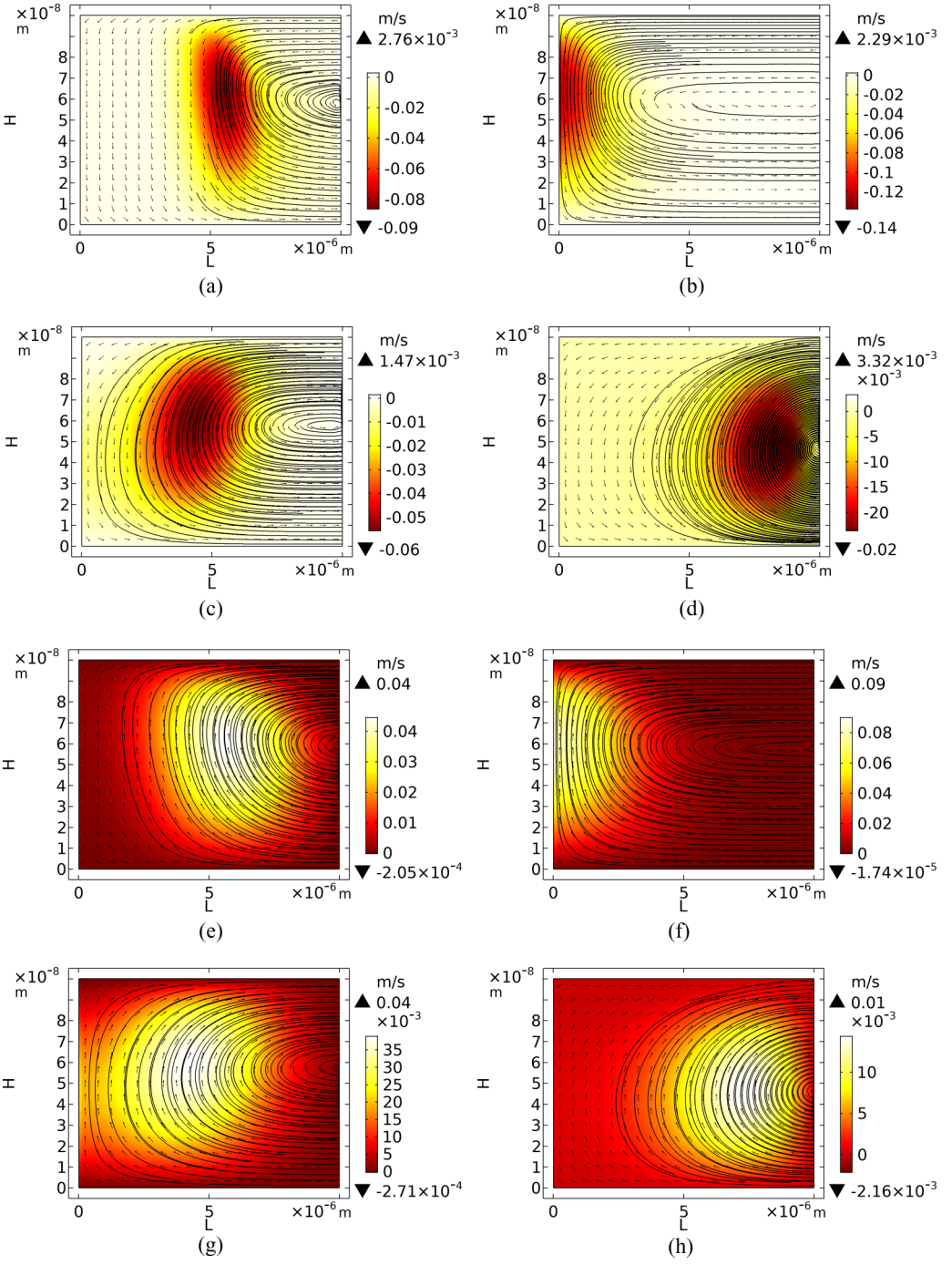

FIG. 15. The solenoidal velocity field in each 1/8 period for ethylene, where the period $T = 1.094 \times 10^{-7}$ s. (a) $t = T/8$; (b) $t = T/4$; (c) $t = 3T/8$; (d) $t = T/2$; (e) $t = 5T/8$; (f) $t = 3T/4$; (g) $t = 7T/8$; (h) $t = T$. The channel conduit half height is 1×10^{-7} m, the length is 1×10^{-5} m. $\rho_e = 52.15\,\mathrm{kg/m^3}$, $T_e = 375\,\mathrm{K}$, $\rho_i/\rho_e = 1.02$, $T_i/T_e = 1.02$.

TABLE I. Ethylene properties used in calculations.

C_p	J/(kg K)	1.799×10^3
C_v	J/(kg K)	1.502×10^3
γ Ratio of heat capacity		1.198
κ Thermal conductivity	W/(m K)	0.0355
μ Shear viscosity	Pa s	1.429×10^{-5}
μ_b Shear viscosity	Pa s	2.700×10^{-3}
T_e Exit temperature	K	375
p_e Exit pressure	Pa	5.807×10^6
ρ_e Exit density	kg/m^3	52.15
c Speed of sound	m/s	365.2
h Half channel height	m	10^{-7}
L Channel length	m	10^{-5}

TABLE II. Nitrogen properties used in calculations.

C_p	J/(kg K)	1.042×10^3
C_v	J/(kg K)	7.44×10^2
γ Ratio of heat capacity		1.40
κ Thermal conductivity	W/(m K)	0.0354
μ Shear viscosity	Pa s	3.19×10^{-5}
μ_b Shear viscosity	Pa s	6.1×10^{-3}
T_e Exit temperature	K	400
p_e Exit pressure	Pa	6×10^6
ρ_e Exit density	kg/m^3	50
c Speed of sound	m/s	344.63
h Half channel height	m	10^{-6}
L Channel length	m	10^{-4}

[1] M. Muskat, *Physical Principles of Oil Production* (McGraw-Hill, New York, 1949).

[2] M. P. Walsh, Oil reservoir primary drive mechanisms, in *Petroleum Engineering Handbook, Vol. V, Reservoir Engineering and Petrophysics*, edited by E. D. Holstein and L. W. Lake (Society of Petroleum Engineers, Richardson, TX, 2007), Chap. 9.

[3] K. P. Chen and D. Shen, Drainage flow of a viscous compressible fluid from a small capillary with a sealed end, J. Fluid Mech. **839**, 621 (2018).

[4] K. P. Chen and D. Shen, Mechanism of fluid production from the nanopores of shale, Mech. Res. Commun. **88**, 34 (2018).

[5] D. Shen and K. P. Chen, Symmetric drainage flow of a compressible fluid from a fracture: analytical solution and slip-like flow rate, Mech. Res. Commun. **99**, 15 (2019).

[6] J. O. Hirschfelder, C. F. Curtiss, and R. B. Bird, *Molecular Theory of Gases and Liquids* (John Wiley & Sons, New York, 1954).

[7] M. J. Lighthill, Viscosity effects in sound waves of finite amplitude, in *Surveys in Mechanics*, edited by G. K. Batchelor and R. M. Davies (Cambridge University Press, Cambridge, New York, 1956).

[8] Annual Energy Outlook 2016 with Projections to 2040, EIA Report No. DOE/ EIA-0383, US Energy Information Administration, Washington, DC, 2016.

[9] S. B. Elbaz, H. Jacob, and A. D. Gat, Transient gas flow in elastic microchannels, J. Fluid Mech. **846**, 460 (2018).
[10] V. Anand and I.C. Christov, On the enhancement of heat transfer and reduction of entropy generation by asymmetric slip in pressure-driven non-Newtonian microflows, J. Heat Transfer **141**, 022403 (2019).
[11] M. Zhang, K. Feng, K. Zhang, Z. Zhao, and Y. Cao, Transient characteristics of a straight tube actuated by viscous compressible flow with consideration of large axisymmetric deformation, Acta Mech. **230**, 105 (2019).
[12] R. L. Panton, *Incompressible Flow*, 4th ed. (Wiley, New York, 2013).
[13] J. Lighthill, *Waves in Fluids* (Cambridge University Press, New York, 1978).
[14] S. Klainerman and A. Majda, Compressible and incompressible fluids, Commun. Pure Appl. Math. **35**, 629 (1982).
[15] R. Klein, Semi-implicit extension of a Godunov-type scheme based on low Mach number asymptotics. I. One-dimensional flow, J. Comput. Phys. **121**, 213 (1995).
[16] C. D. Munz, S. Roller, R. Klein, and K. J. Geratz, The extension of incompressible flow solvers to the weakly compressible regime, Comput. Fluids **32**, 173 (2003).
[17] C. D. Munz, M. Dumbser, and S. Rolle, Linearized acoustic perturbation equations for low Mach number flow with variable density and temperature, J. Comput. Phys. **224**, 352 (2007).
[18] Y. Jin and K. P. Chen, Fundamental equations for primary fluid recovery from porous media, J. Fluid Mech. **860**, 300 (2019).
[19] R. Aris, *Vectors, Tensors, and the Basic Equations of Fluid Mechanics* (Dover Publications, New York, 1989).
[20] L. G. Leal, *Advanced Transport Phenomena* (Cambridge University Press, New York, 2010).
[21] A. D. Pierce, *Acoustics: An Introduction to Its Physical Principles and Applications* (McGraw-Hill, New York, 1981).
[22] W. M. Beltman, Viscothermal wave propagation including acousto-elastic interaction, part I: theory, J. Sound Vibr. **227**, 555 (1999).
[23] P. M. Morse and K. Uno Ingard, *Theoretical Acoustics* (McGraw-Hill, New York, 1968).
[24] M. J Buckingham, Causality, Stokes' wave equation, and acoustic pulse propagation in a viscous fluid, Phys, Rev. E **72**, 026610 (2005).
[25] D. G. Crighton, Model equations of nonlinear acoustics, Annu. Rev. Fluid Mech. **11**, 11 (1979).
[26] COMSOL Multiphysics® Modeling Software (Burlington, MA, 2016).